

Integrated Sliding-Mode Sensorless Driver with Pre-driver and Current Sensing Circuit for Accurate Speed Control of PMSM

Sewan Heo, Jimin Oh, Minki Kim, Jung-Hee Suk, Yil Suk Yang, Ki-Tae Park, and Jinsung Kim

This paper proposes a fully sensorless driver for a permanent magnet synchronous motor (PMSM) integrated with a digital motor controller and an analog pre-driver, including sensing circuits and estimators. In the motor controller, a position estimator estimates the back electromotive force and rotor position using a sliding-mode observer. In the pre-driver, drivers for the power devices are designed with a level shifter and isolation technique. In addition, a current sensing circuit measures a three-phase current. All of these circuits are integrated in a single chip such that the driver achieves control of the speed with high accuracy. Using an IC fabricated using a 0.18 μm BCDMOS process, the performance was verified experimentally. The driver showed stable operation in spite of the variation in speed and load, a similar efficiency near 1% compared to a commercial driver, a low speed error of about 0.1%, and therefore good performance for the PMSM drive.

Keywords: Sensorless control, sliding-mode observer, SMO, back-EMF estimation, speed error, PMSM, BLDC motor.

Manuscript received Apr. 21, 2015; revised Aug. 19, 2015; accepted Sept. 7, 2015.

This research was supported by the IT R&D program of MKE/KEIT, Rep. of Korea (10035171, Development of High Voltage/Current Power Module and ESD for BLDC Motor).

Sewan Heo (corresponding author, sewany@etri.re.kr) is with the IT Convergence Technology Research Laboratory, ETRI, Daejeon, Rep. of Korea.

Jimin Oh (ojmhiin@etri.re.kr), Minki Kim (mkk@etri.re.kr), Jung-Hee Suk (jhsuk@etri.re.kr), and Yil Suk Yang (ysyang@etri.re.kr) are with the Information & Communications Core Technology Research Laboratory, ETRI, Daejeon, Rep. of Korea.

Ki-Tae Park (kt2000.park@irondevice.com) and Jinsung Kim (npstar@irondevice.com) are with the Iron Device Corporation, Seoul, Rep. of Korea.

I. Introduction

Motors of different types have been used in many industry applications and home appliances. There are dc and ac motors, and ac motors are divided into induction and synchronous motors. The induction motor is most commonly used in industry because it is durable and does not require controls, despite its low efficiency. The brushless direct current (BLDC) motor and permanent magnet synchronous motor (PMSM), representatives of synchronous motors, require a complex control for synchronization to the rotor position. However, they have a high efficiency and can operate at a constant speed regardless of the load.

A synchronous motor uses a position sensor to detect the exact rotor position. The encoder or resolver is accurate but has a large volume, and the hall sensor should be embedded in the motor. Thus, many researches on motor control without a position sensor have been conducted [1]–[2]. The position sensorless control of a BLDC motor is based on the detection of the back electromotive force (back-EMF) generated by the motor rotation [3]–[4]. In this case, the back-EMF can be measured from a floating phase during the trapezoidal drive for the BLDC motor. Meanwhile, for sensorless control of the PMSM, the back-EMF should be estimated through certain techniques, because it cannot be measured owing to the sinusoidal drive with no floating phase.

A sliding-mode observer (SMO) is commonly used for the back-EMF estimation of a PMSM [5]–[8]. This technique estimates the current corresponding to the voltage based on an equivalent motor model, and then estimates the back-EMF

from the error between the estimated current and the actual current. The error decreases by applying the back-EMF to the model; thus, the estimated current tracks the actual current in sliding mode. There are three switching functions for the sliding mode. The *sigum* function is simple but causes chattering and delay from a low-pass filter [8]. The *saturation* function [6] and the *sigmoid* function [5] are used instead to avoid the chattering problem.

For an accurate estimation of the back-EMF, an accurate measurement, precise parameters of the motor model, and a stability analysis are required. The actual voltage, by compensating the dead-time caused by a modulation, can improve the estimation accuracy [6]. Online parameter detection for a higher precision can also achieve a higher estimation accuracy [9], but there become many variables in the system. A stability analysis is also necessary for a stable sensorless control [5]. These are very important because an inaccurate estimation of the rotor position may cause a failure of the synchronization to the rotation. On the other hand, a separate start-up technique is required because the back-EMF cannot be estimated or measured at the initial state with no rotation [8].

Most controllers are generally implemented with a digital signal processor [3]–[7]. A non-fabricated field-programmable gate array [8], or a processor with a partially fabricated circuit for sensorless control [10], was introduced. These are not implemented with a full fabrication, which can maximize the driver performance. In addition, position-sensorless drive with a speed sensor or a current sensor [11] is not completely sensorless. Thus, in this paper, a fully fabricated and fully sensorless driver is proposed. The motor controller is implemented using a digital circuit to run a complex algorithm within a small area, and a pre-driver with a sensing circuit is

integrated with the controller to increase the accuracy of the speed control without a duty ratio distortion of the PWM signal. It is stable under an abrupt variation of the speed and load, as efficient as a control using a position sensor, and has a low speed ripple and error with an accurate speed control. A sensorless driver for a PMSM, integrated with a pre-driver and a three-phase current sensing circuit and fabricated in a single chip, has not been introduced yet. Through this sensorless driver, a high speed control accuracy and efficiency can be achieved with high stability.

II. System Architecture

A PMSM drive system consists of a motor controller, a pre-driver, and an inverter. A block diagram of the proposed integrated sensorless motor driver is presented in Fig. 1. It is a mixed-mode united circuit composed of a motor controller, in which a sensorless algorithm is implemented by a digital circuit, and a pre-driver with a current sensing circuit implemented by an analog circuit. The proposed driver can drive high power to a PMSM through a three-phase inverter.

The motor controller is composed of a position estimator, a speed controller, and a voltage modulator. The position estimator estimates the back-EMF from the three-phase voltage and current information of the motor, and calculates the rotor position from the back-EMF. The speed controller estimates the rotation speed from the variation of the rotor position, and determines the phase voltage as a modulation index by comparing with a reference speed. The speed estimator counts the exact time interval from the main system clock to increase the accuracy of the speed control, an adaptive time of the modulation index change is used to reduce the speed ripple, and the modulation index has a high resolution to

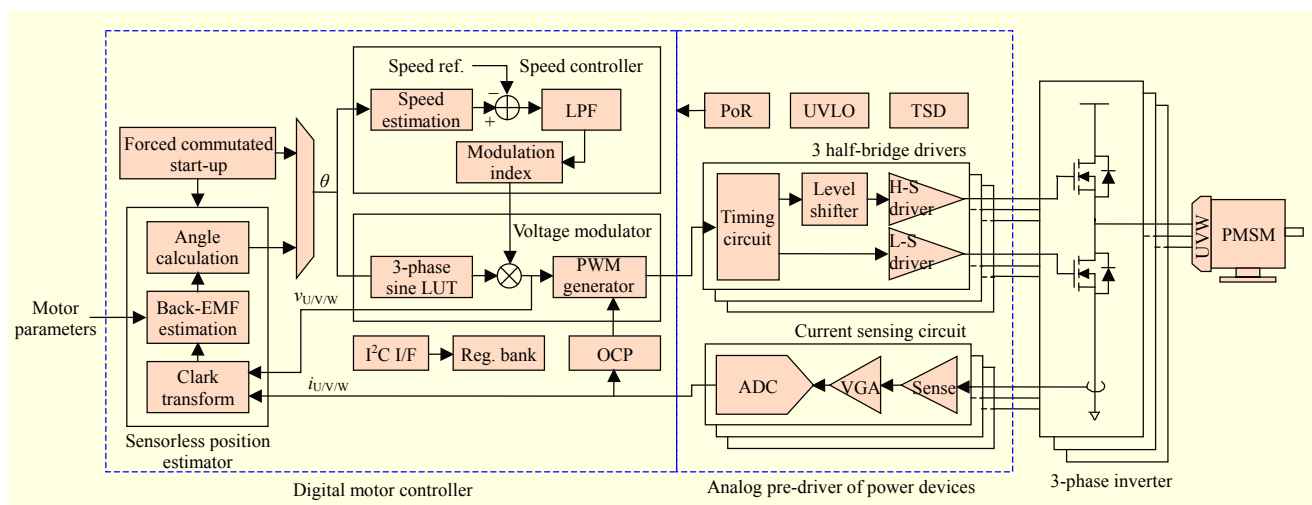


Fig. 1. Motor drive system of proposed integrated sensorless motor driver.

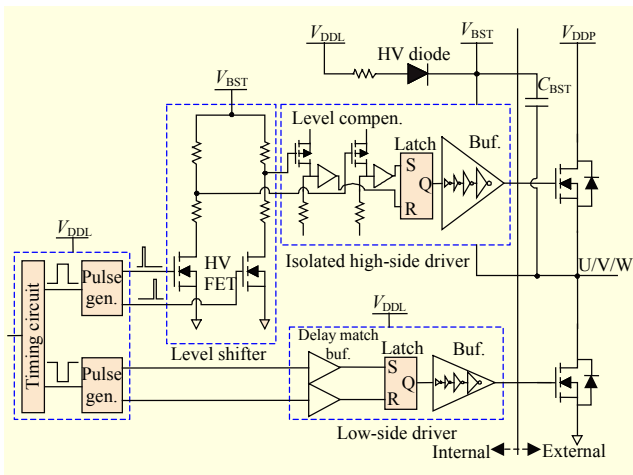


Fig. 2. Pre-driver circuit for one phase.

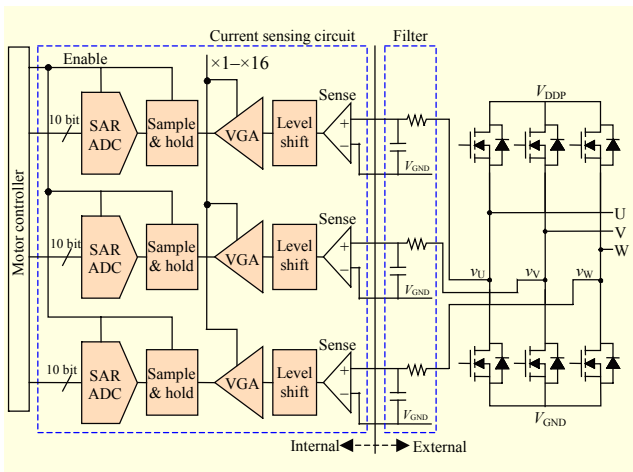


Fig. 3. Three-phase current sensing circuit.

reduce the speed error. The voltage modulator finds the proper three-phase voltage combination corresponding to the rotor position in the sine look-up table (LUT), scales the voltage according to the modulation index, and outputs the final PWM signal by comparing to a saw wave. In the LUT, a third harmonic wave is added to the pure sinusoidal waves to maximize the fundamental amplitude with the same PWM voltage as described in [12].

A pre-driver is necessary to transmit the PWM signal generated in the controller to the inverter, changing the signal from a low voltage level to a high level. A detailed circuit of the pre-driver for one phase is shown in Fig. 2. The most important feature is that a level shifter, which can be integrated in a circuit and make the high voltage level, is used to drive a high-side power device through a bootstrap technique. First, the PWM signal is divided into two signals for the high and low sides after adding the dead-time. To prevent a considerable amount of current consumption, two pulse signals are generated for

each side, and the signals for the high side are transmitted to the level shifter. After changing the level to high, they are compensated based on the level of change. Because the pulse signals are only available for a short time, a set-reset (SR) latch holds the output for the high-side driver.

There are two voltage domains in the pre-driver. One is a low voltage (V_{DDL}) for the pulse signal generation and low-side driver, and the other is the bootstrap voltage (V_{BST}) of the high voltage for the level shifter and high-side driver. Thus, some high-voltage devices are used in the level shifter and the bootstrap diode, whereas the high-side driver adopts isolated transistors that have a floating ground tied to the inverter output. Because all components of this pre-driver, except the capacitors for the bootstrap, are integrated with the motor controller, the PWM signal generated from the controller can be transmitted to the inverter without a duty ratio distortion.

An accurate current sensing technique with a high resolution is required to increase the stability of the sensorless control and the performance of the speed control [1]. Figure 3 shows the current sensing circuit including three independent 10-bit analog-to-digital converters (ADCs) for concurrently sensing a three-phase current flowing through the power devices. Because the motor current flows through the low-side power devices regardless of the current direction, it is measured based on their voltage drops, as described in [4], and further measured concurrently when all of the power devices are turned on. Although this can be done through an additional series resistor to improve the accuracy, it has the problem of an efficiency degradation. The voltage drop is sensed as a signal by the circuit through a filter. Because it is either positive or negative according to the current direction, the signal level is increased by the level shifter. The signal is then amplified using a variable gain amplifier (VGA) with a gain considering the resistance of the power device. The ADC, which is enabled only when all low-side power devices are turned on, samples and holds the signal, and then converts it into a digital value using a successive approximation register (SAR) method. Finally, it is used for the sensorless algorithm and over current protection (OCP) in the motor controller.

The phase current varies not smoothly but roughly by the pulse shape of the PWM voltage, as shown in Fig. 4. The motor drive system in Fig. 1 was simulated with actual parameters by Power Sim simulator. Figure 4(a) shows the current ripple of more than 1 A of the three phases at 3,000 rpm under a light load condition. An accurate current measurement seems to be limited by the ripple. However, the three independent ADCs can operate simultaneously at a requested time when all low-side power devices are turned on, as shown in Fig. 4(b). Because they are integrated and synchronized with the PWM signal, the measurement errors are minimized. The

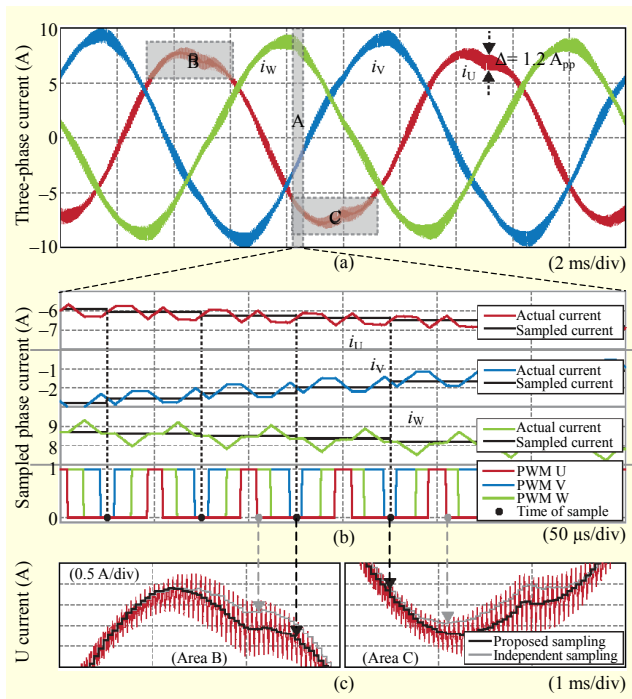


Fig. 4. Simulated current measurement by sampling of ADCs: (a) three-phase current, (b) simultaneous sampling, and (c) effect of proposed sampling.

simultaneous sampling of the current has a good performance, as shown in Fig. 4(c), compared to the independent sampling for each phase. The measurements of the three-phase current at different times lower the accuracy of the measured value.

III. Sensorless Control with Back-EMF Estimation

1. SMO

There are many methods of back-EMF estimation for sensorless control because the back-EMF cannot be measured directly from the motor. SMO is a back-EMF estimation method and entails a minimization of the errors between the estimated current and actual current based on the equivalent motor model. The estimated current tracks the actual current in sliding mode. The phase current is estimated using the phase voltage and estimated back-EMF because it varies by two factors in the motor. From the current state of the phase current, voltage, and back-EMF, the next state can be estimated; and the estimation can then be done recursively. The phase voltage is easily obtained from the integrated control blocks, not from the measurement, and the actual phase current is measured by the current sensing circuit.

In the equivalent model of the PMSM shown in Fig. 5, three phases — U, V, and W — have a star (Y) connection and a neutral point, N . Each phase current flows through a resistor,

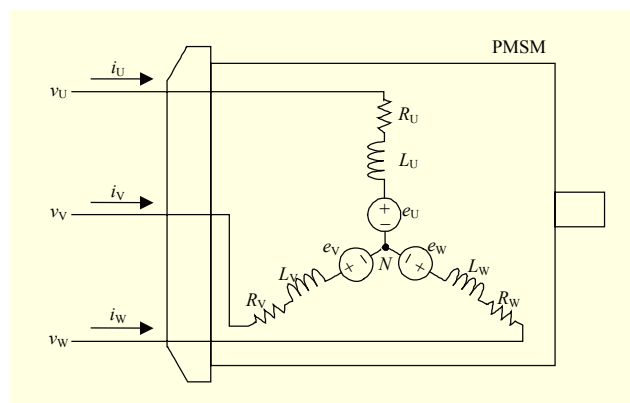


Fig. 5. Equivalent model of PMSM.

an inductor, and a back-EMF when the corresponding phase voltage is applied. It is assumed that the three phases each have the same resistance and inductance, and each phase can be analyzed independently as neutral point N is a virtual ground in the case of a sinusoidal drive [4]. For the rotor position, the rotor angle can be defined using the three axes, located at every 120 degrees in the stator, for the U, V, and W phases. However, it can also be defined using two orthogonal axes for α and β phases after a Clark transformation [11] for a simple analysis of the rotor angle.

For the two phases of α and β in a fixed frame, the relations among the phase voltage, current, and back-EMF can be represented as state equations, where the phase current is a state variable. These voltage equations can be represented as

$$\begin{aligned} \dot{i}_\alpha &= -\frac{R}{L}i_\alpha - \frac{1}{L}e_\alpha + \frac{1}{L}v_\alpha, \\ \dot{i}_\beta &= -\frac{R}{L}i_\beta - \frac{1}{L}e_\beta + \frac{1}{L}v_\beta, \end{aligned} \quad (1)$$

where R is the phase resistance, L is the phase inductance, and $v_{\alpha/\beta}$, $i_{\alpha/\beta}$, and $e_{\alpha/\beta}$ are the voltage, current, and back-EMF for each phase, respectively. According to (1), the next state of the phase current is estimated through the input voltage, input back-EMF, and current state of the phase current. In this case, the input back-EMF is estimated through the SMO.

2. Back-EMF Estimation

The sensorless algorithm for back-EMF estimation based on SMO is shown in Fig. 6. Initially, the voltage and current are normalized to adjust the scales to each other. Through a Clark transform, $v_{\alpha/\beta}$ and $i_{\alpha/\beta}$ are obtained from the three-phase voltage and current, which are used for the back-EMF estimation. Because the estimated current and estimated back-EMF are used in the SMO, the state equations of (1) can be changed as follows:

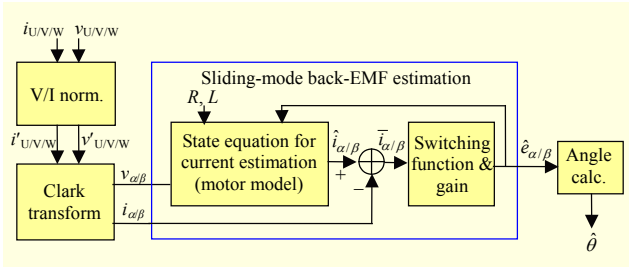


Fig. 6. Sensorless control algorithm based on SMO.

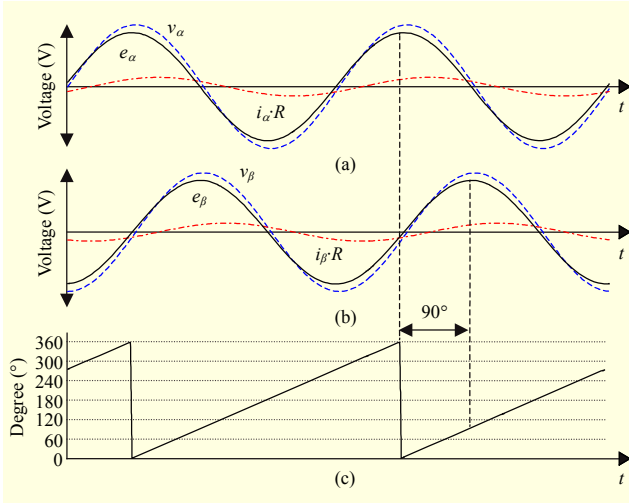


Fig. 7. Back-EMF estimation from transformed phase voltage and current: (a) α -phase, (b) β -phase, and (c) estimated rotor angle.

$$\begin{aligned}\hat{i}_\alpha &= -\frac{R}{L}\hat{i}_\alpha - \frac{1}{L}\hat{e}_\alpha + \frac{1}{L}v_\alpha, \\ \hat{i}_\beta &= -\frac{R}{L}\hat{i}_\beta - \frac{1}{L}\hat{e}_\beta + \frac{1}{L}v_\beta,\end{aligned}\quad (2)$$

where $\hat{i}_{\alpha/\beta}$ and $\hat{e}_{\alpha/\beta}$ are the estimated current and back-EMF, respectively. The error $\bar{i}_{\alpha/\beta}$, which is the difference between the estimated current and actual current, determines the estimated back-EMF through a switching function and amplification, which can be represented as

$$\begin{aligned}\hat{e}_\alpha &= kS(\bar{i}_\alpha) = kS(\hat{i}_\alpha - i_\alpha), \\ \hat{e}_\beta &= kS(\bar{i}_\beta) = kS(\hat{i}_\beta - i_\beta),\end{aligned}\quad (3)$$

$$S(x) = \begin{cases} x & \text{for } -1 < x < 1, \\ -1 & \text{for } x \leq -1, \\ 1 & \text{for } x \geq 1, \end{cases}\quad (4)$$

where k is the observer gain, which is determined to be appropriate and large enough for the stability, and S is the saturation function. Substituting (3) into (2), the final state equations, which have only two inputs of voltage and actual current, can be represented as

$$\begin{aligned}\dot{\hat{i}}_\alpha &= -\frac{R}{L}\hat{i}_\alpha - \frac{1}{L}kS(\hat{i}_\alpha - i_\alpha) + \frac{1}{L}v_\alpha, \\ \dot{\hat{i}}_\beta &= -\frac{R}{L}\hat{i}_\beta - \frac{1}{L}kS(\hat{i}_\beta - i_\beta) + \frac{1}{L}v_\beta,\end{aligned}\quad (5)$$

where the estimated current is the state variable.

Assuming that the estimated current almost tracks the actual current, (2) can be simplified as

$$\begin{aligned}\hat{e}_\alpha &= v_\alpha - Ri_\alpha, \\ \hat{e}_\beta &= v_\beta - Ri_\beta.\end{aligned}\quad (6)$$

According to the voltage equation of (6), Fig. 7 shows that the back-EMF can be estimated by the voltage and current for the α and β phases, and that the rotor position is calculated from the two back-EMF waves. The back-EMF is determined by the phase voltage and voltage drop by the current through the resistance. Because α and β have a phase difference of 90 degrees, the two back-EMF waves also have the same difference. Meanwhile, the rotation speed is estimated from the variation of the rotor position. Thus, the estimated rotor position and speed can be represented, respectively, as

$$\hat{\theta} = -\tan^{-1}\left(\frac{\hat{e}_\alpha}{\hat{e}_\beta}\right), \quad \hat{\omega} = \frac{d}{dt}\hat{\theta}.\quad (7)$$

Driving a motor using the estimated back-EMF by the SMO requires a stability analysis of the control for stable operation. Considering the estimation error between the estimated current and actual current as a sliding surface, the Lyapunov function [5] can be defined as

$$V = \frac{1}{2}(\bar{i}_\alpha^2 + \bar{i}_\beta^2).\quad (8)$$

The sliding mode exists when $\dot{V} < 0$; the differential function of (8) can be represented as

$$\dot{V} = \bar{i}_\alpha \dot{\bar{i}}_\alpha + \bar{i}_\beta \dot{\bar{i}}_\beta = \bar{i}_\alpha(\dot{\hat{i}}_\alpha - \dot{i}_\alpha) + \bar{i}_\beta(\dot{\hat{i}}_\beta - \dot{i}_\beta).\quad (9)$$

Substituting (1), (2), and (3) into (9), this can be simplified as

$$\begin{aligned}\dot{V} &= -\frac{R}{L}\bar{i}_\alpha^2 - \frac{1}{L}\bar{i}_\alpha(kS(\bar{i}_\alpha) - e_\alpha) \\ &\quad - \frac{R}{L}\bar{i}_\beta^2 - \frac{1}{L}\bar{i}_\beta(kS(\bar{i}_\beta) - e_\beta),\end{aligned}\quad (10)$$

Finally, the condition for the existence of the sliding mode is obtained as

$$k \geq |e_\alpha|, \quad k \geq |e_\beta|,\quad (11)$$

where k is the observer gain. Therefore, the observer gain should be determined to be large enough for the stability of the SMO.

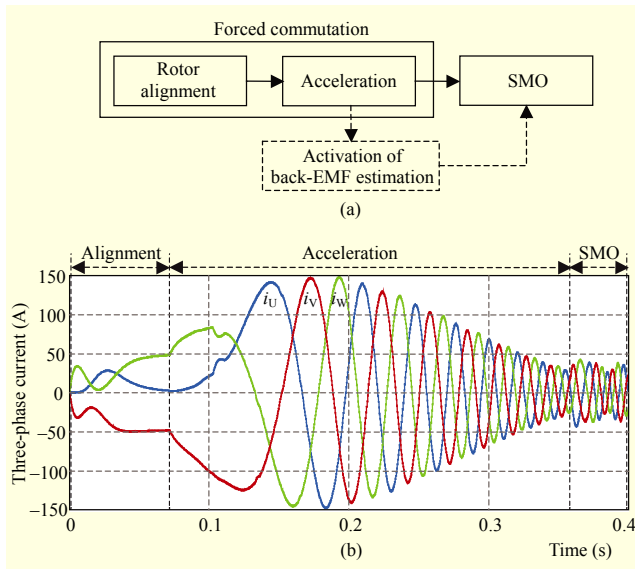


Fig. 8. Forced commutated start-up: (a) block diagram and (b) simulated three-phase current waveform.

3. Start-Up

An estimation of the rotor is difficult when the rotor does not rotate or rotates slowly because the back-EMF is generated by the rotation, and the amplitude is proportional to the rotation speed. Thus, among some start-up techniques for the initial sensorless drive, Fig. 8 shows a forced commutation technique with an open-loop control, which is generally used. The rotor is initially aligned by driving a predetermined point. Next, the point moves and circulates slowly so that the rotor rotates following the point without recognizing the exact rotor position, and the circulation is accelerated with an increasing modulation index. During the forced commutation, the back-EMF can be estimated by the SMO. When the speed reaches a predetermined value during the acceleration, the sensorless drive finally changes the control from the forced commutation to the SMO. Figure 8 shows the three-phase current during the start-up according to the sequence. The rotor becomes located at a specific point based on its alignment. Although the initial current is large, it becomes stable through the acceleration. Therefore, the sensorless drive becomes complete by adding the start-up technique to the SMO algorithm.

IV. Experimental Results

The proposed integrated sensorless driver was constructed by combining a digital motor controller and an analog pre-driver in a single chip including electrostatic discharge protection circuits [13], as shown in Fig. 9. It was fabricated using a $0.18\ \mu\text{m}$ BCDMOS process in a $13.2\ \text{mm}^2$ area. Table 1 shows

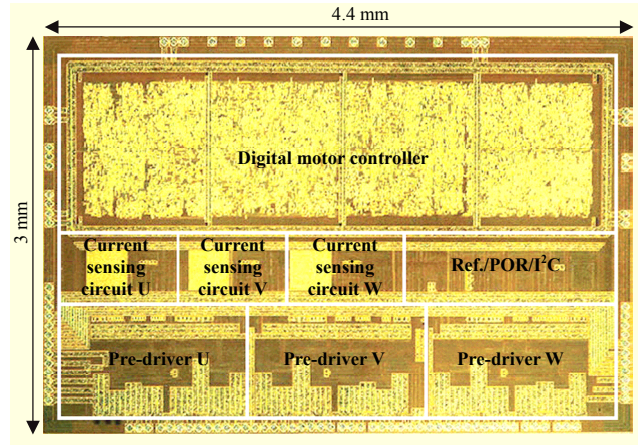


Fig. 9. Microphotograph of integrated driver chip.

Table 1. Characteristics of proposed driver.

| | Digital motor controller | Analog pre-driver |
|-------------------|--------------------------|--|
| Operating voltage | 1.8 V | 5 V |
| Operating current | 5 mA | 11 mA (driver) * 4.5 mA (current sensing) |
| Frequency | 20 MHz (main clock) | 20 kHz (PWM switching) |

* The drive current for power devices is not included.

Table 2. Specifications of PMSM.

| Motor ratings | | Phase parameters | |
|-----------------|-----------|-------------------|------------|
| Output power | 1,500 W | Inductance | 0.1 mH |
| Torque | 4.8 N·m | Resistance | 17 mΩ |
| Voltage | 48 V | Torque constant | 0.06 N·m/A |
| Current | 33 A | Back-EMF constant | 6 V/krpm |
| Speed | 3,000 rpm | N/A | N/A |
| Number of poles | 4 | N/A | N/A |

the characteristics of the driver. The digital circuit and analog circuit used 1.8 V and 5 V, and operated at 20 MHz and 20 kHz, respectively. The main clock was divided by 1,000 to generate the PWM switching frequency.

The three-phase inverter was made using power MOSFETs having a break-down voltage of 100 V. As shown in Table 2, a PMSM, having an output power of 1,500 W with a rated voltage of 48 V and rated current of 33 A, was used. In the experiment, the motor operated at 1,000 rpm, 2,000 rpm, and 3,000 rpm under a load less than 5 N·m, and the function was verified in the environment, as shown in Fig. 10(a). The proposed driver IC, composed of a motor controller and pre-driver, drove a PMSM coupled with a hysteresis brake though a three-phase inverter. The driver was configured with motor

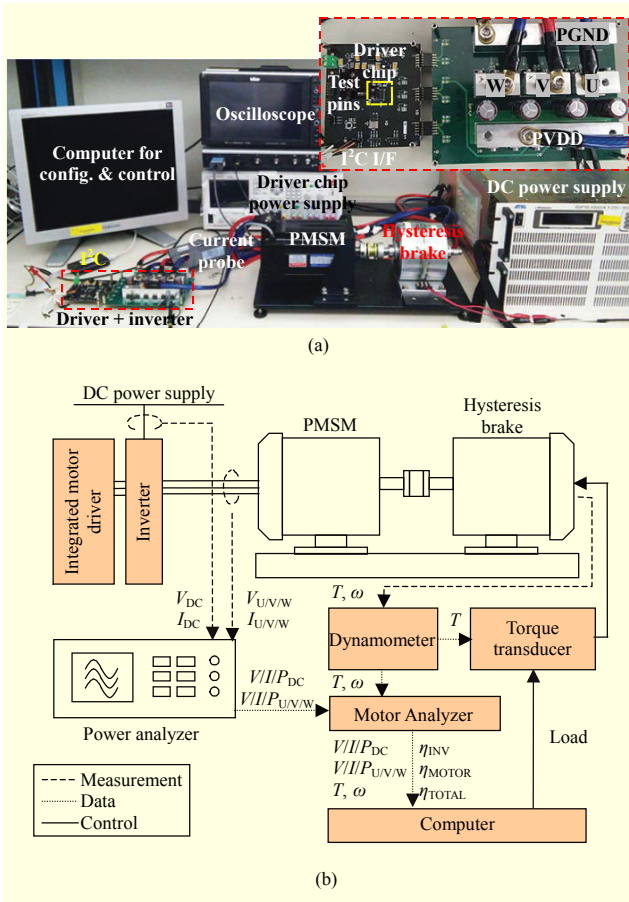


Fig. 10. Environment for experiment: (a) function verification and (b) performance evaluation.

parameters and controlled for a speed change by a computer through an I²C serial interface. The phase current and voltage were measured by an oscilloscope. Moreover, internal signals in the driver, such as sensed actual current, estimated current, estimated back-EMF, estimated rotor angle, and estimated speed, were also measured during the sensorless control through test-pin outputs of the driver. The function was verified by measuring the control status and operation signals in the driver under speed and load variation.

The performance was evaluated in the environment shown in Fig. 10(b) including the environment for function verification. All phase voltages, currents, and power levels of the motor were measured and calculated by a power analyzer; the speed and torque were measured by a dynamometer, and this information was transmitted to a motor analyzer. The motor analyzer calculated efficiency using the power levels of the power supply and each phase, as well as using the rotation status. The efficiency was analyzed in the motor analyzer for three types; that is, the inverter efficiency, η_{INV} , motor efficiency, η_{MOTOR} , and total efficiency, η_{TOTAL} , which are represented as

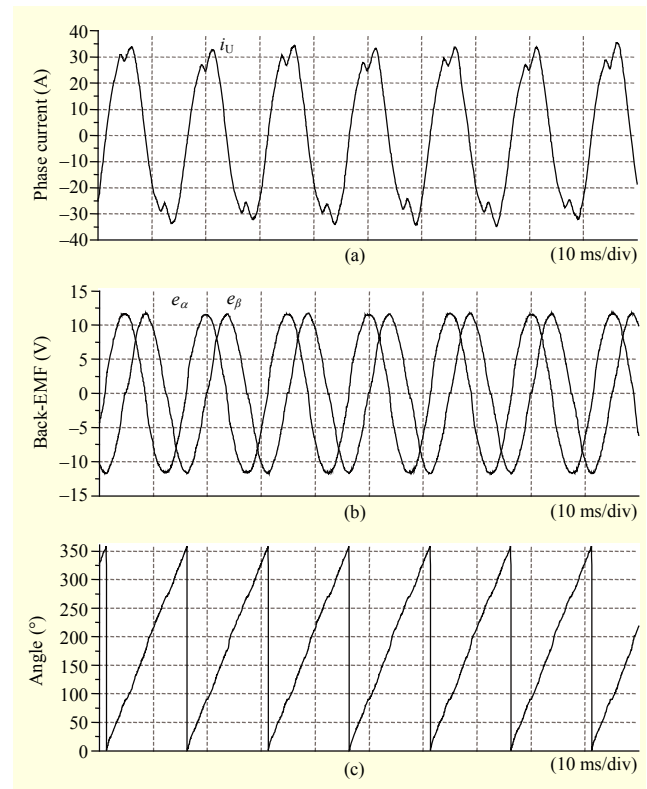


Fig. 11. Measured waveform at 2,000 rpm under 3 N·m load: (a) U-phase current, (b) internal estimated back-EMF signal in driver, and (c) internal estimated rotor angle signal in driver.

$$\eta_{INV} = P_{AC} / P_{DC} = \sum P_{U/V/W} / (V_{DC} \times I_{DC}),$$

$$\eta_{MOTOR} = P_{OUT} / P_{AC} = (\omega \times T) / \sum P_{U/V/W}, \quad (12)$$

$$\eta_{TOTAL} = \eta_{INV} \times \eta_{MOTOR} = P_{OUT} / P_{DC},$$

where V_{DC} and I_{DC} are the voltage and current of the dc power supply, and ω and T are the angular speed and torque of the motor, respectively. These data were transmitted to a computer and recorded. During the experiment, the computer made a torque transducer to increase the load from zero to the rated torque in small steps. For each step, all measured and calculated data including the efficiency were recorded.

The phase current waveform is generally used to confirm the motor operation. It is also used to show the speed (based on the frequency) and load (based on an estimate of the amplitude). Figure 11(a) shows a measured one-phase current at 2,000 rpm under a 3 N·m load. The estimated back-EMF signal and estimated rotor position signal by the SMO are shown in Figs. 11(b) and 11(c), respectively, which were measured from the driver through the test-pin outputs. It was verified that the sensorless algorithm can estimate the back-EMF and drive the motor with the calculated rotor position.

The stability of the sensorless drive was confirmed, as shown in Fig. 12, based on the speed variation when the reference

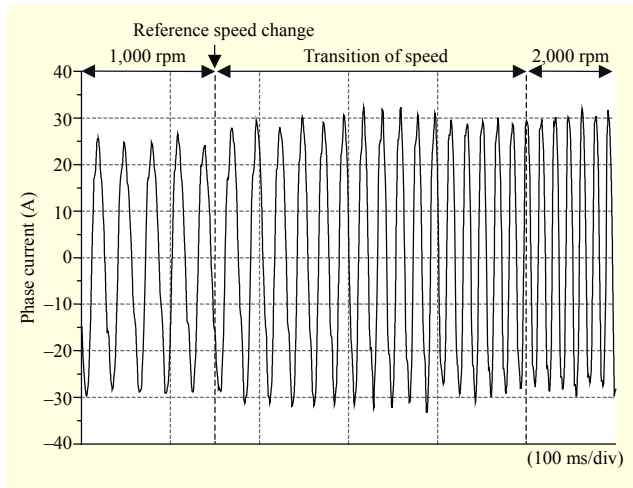


Fig. 12. Measured phase current at speed change from 1,000 rpm to 2,000 rpm under constant 3 N-m load with sensorless control.

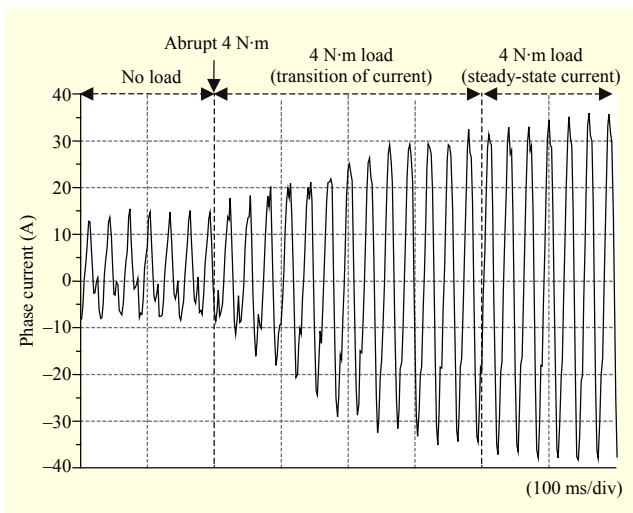


Fig. 13. Measured phase current at load change from 0 N-m to 4 N-m at constant 1,000 rpm with sensorless control.

speed changes abruptly. The speed increased from 1,000 rpm to 2,000 rpm for 0.35 s under a constant 3 N-m load; thus, the frequency of the current also increased two-fold and the amplitude became slightly larger. The driver was thus verified to be robust under a speed variation.

The stability was confirmed once again, as shown in Fig. 13, by an abrupt load variation. The load was increased from 0 N-m to 4 N-m at a constant 1,000 rpm. The speed became lower at the time of the increase, but the driver soon recovered its speed. The amplitude became larger owing to the increased load, and it took 0.4 s to reach a steady state. Because the speed was maintained, the driver was thus verified to be robust under a load variation. The robustness under both a speed and a load variation means that the back-EMF was estimated in the SMO

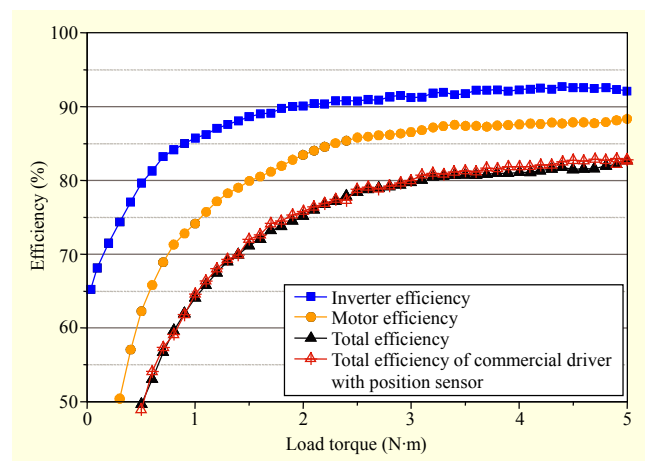


Fig. 14. Measured inverter, motor, and total efficiency of sensorless driver at constant 2,000 rpm, and comparison with commercial driver using sensed control.

exactly by applying all transitions of the current and voltage.

The most important performance factor of the motor drive is generally the efficiency. The inverter, motor, and total efficiency were measured according to (12), as shown in Fig. 14, while the motor operated at a speed of 2,000 rpm under a rated load of 5 N-m using sensorless control. The inverter efficiency was over 85% in most of the load range, and showed a maximum of 93%. This can be obtained only when the active ac power is larger than the reactive power, owing to a small phase difference between the voltage and current. Although the motor efficiency was relatively small at a light load, it was increased as the load became closer to the rated load, and showed a maximum of 88%. Owing to the high inverter efficiency, the total efficiency was also high.

For an evaluation of the efficiency of the sensorless driver, another total efficiency, shown in Fig. 14 for comparison purposes, was measured using a commercial driver with a position sensor, and the same motor at the same speed and load condition. The two total efficiencies showed at most only a 1% difference in all load ranges, and the proposed sensorless driver had a slightly lower efficiency at a heavier load than the commercial driver using a position sensor. Therefore, the proposed sensorless driver has a good performance compared to the driver under sensed control.

The motor is driven by a combination of the three-phase current, which is not constant but sinusoidal. The rotor rotates based on the sum of the three-phase torque, which is generated by the overlap of the three-phase current and back-EMF. Because the torque sum is not even, the rotation speed is variable, and this shows near the reference speed. This variation makes the speed ripple (ω_{ripple}) and speed error (ω_{err}), which can be defined as

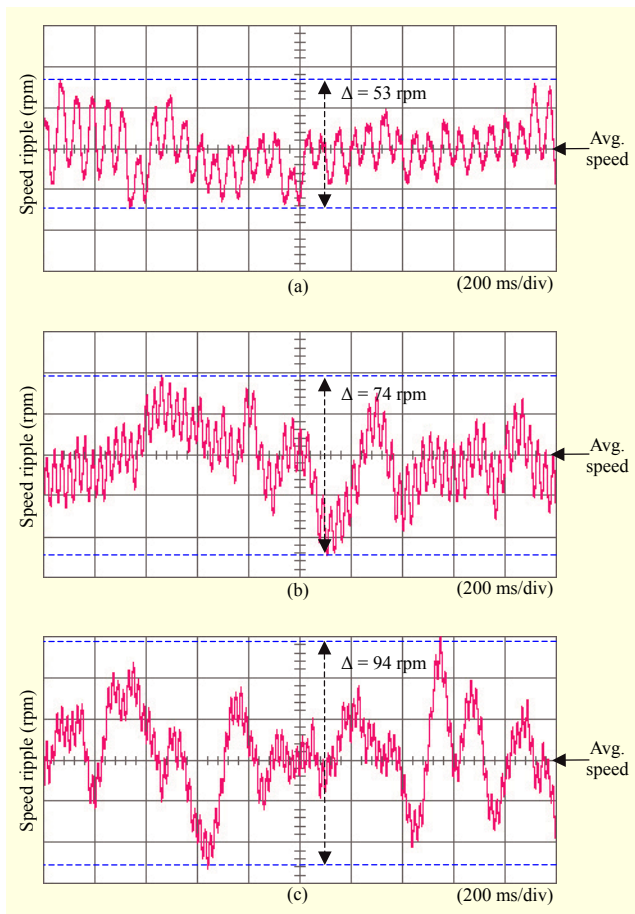


Fig. 15. Measured speed ripples: (a) 1,000 rpm, (b) 2,000 rpm, and (c) 3,000 rpm.

$$\omega_{\text{ripple}} = (\omega_{\text{max}} - \omega_{\text{min}}) / \omega_{\text{avg}}, \quad (13)$$

$$\omega_{\text{err}} = (\omega_{\text{avg}} - \omega_{\text{ref}}) / \omega_{\text{ref}},$$

where ω_{max} , ω_{min} , ω_{avg} , and ω_{ref} are the maximum speed, minimum speed, average speed, and reference speed, respectively. The speed ripples were measured by a rotation vibrometer at 1,000 rpm, 2,000 rpm, and 3,000 rpm, as shown in Fig. 15. The speed ripples of 53 rpm, 74 rpm, and 94 rpm were measured at 1,000 rpm, 2,000 rpm, and 3,000 rpm, respectively, and were 5.3%, 3.7%, and 3.1%, respectively, as a percentage of each average speed. They became smaller when the average speed increased. They were measured under no load to exclude the influence of a load, but the results were similar at medium and full load conditions. The speed ripples were moderate compared to previous works, as shown in Table 3, considering that [14]–[16] used both a position sensor and a speed sensor, and that only [17] was based on a sensorless control.

The speed error is also an important performance factor of the speed control. According to (13), the speed error is small when the average speed is close to the reference speed. The

Table 3. Comparison of speed ripple and error with previous works.

| | Speed ripple | Speed error | Speed (rpm) | Motor type |
|-----------|--------------|-------------|-------------|------------|
| 2007 [14] | 3.4% | 0.4% | 1,000 | BLDCM |
| 2009 [15] | 1.2% | 0.12% | 2,500 | BLDCM |
| 2010 [16] | 6.0% | N/A | 500 | SRM |
| 2011 [17] | 3.7% | N/A | 1,800 | SRM |
| 2014 [18] | 3.5% | 0.2% | 1,000 | PMSM |
| This Work | 3.1% | 0.07% | 3,000 | PMSM |
| | 3.7% | 0.1% | 2,000 | |
| | 5.3% | 0.14% | 1,000 | |

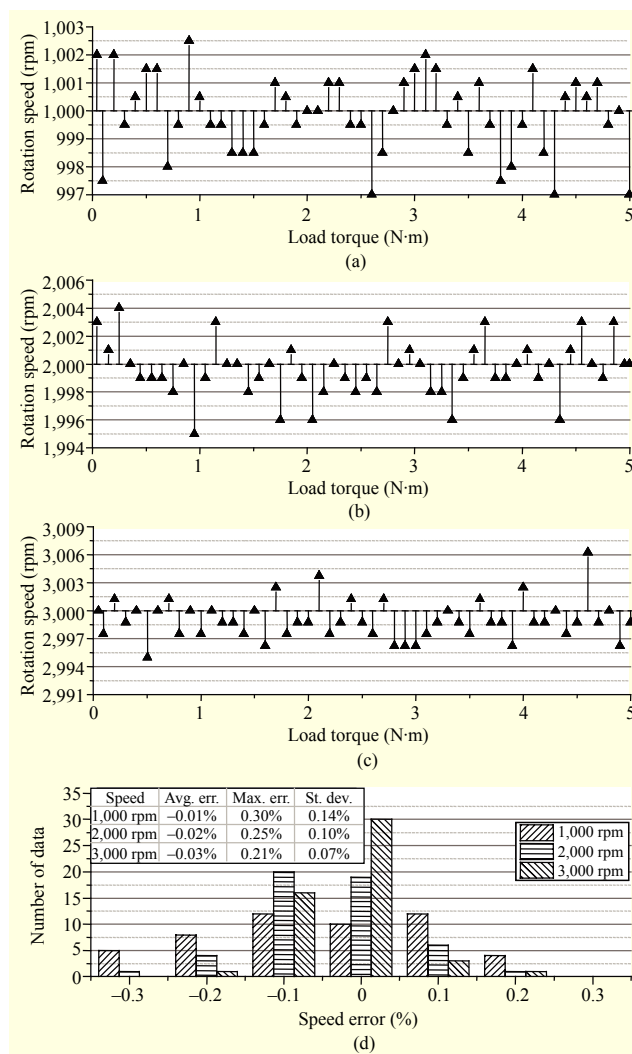


Fig. 16. Measured speed error at all load ranges: (a) 1,000 rpm, (b) 2,000 rpm, (c) 3,000 rpm, and (d) histogram.

speed errors were measured at 1,000 rpm, 2,000 rpm, and 3,000 rpm under a load of 5 N·m, as shown in Fig. 16. The speed errors were similar at each speed regardless of the load

because the modulation index of the controller had a high resolution at any load. The absolute maximum errors at 1,000 rpm, 2,000 rpm, and 3,000 rpm were 3 rpm, 5 rpm, and 6 rpm, respectively, as shown in Figs. 16(a), 16(b), and 16(c).

Most of the errors, however, were very small for all loads, which is evident from the histogram in Fig. 16(d). All speed errors of the three speeds were within $\pm 0.3\%$, and they seemed to show normal distributions because the amount of data increased as the error became closer to 0%. The absolute speed difference was large at a high speed, but the percentage became small because of the division by the high reference speed. Thus, the amount of data on zero speed errors at 3,000 rpm was greater than at 1,000 rpm. For all speeds and loads, the average error was within 0.03%, the maximum error was within 0.3%, and the statistical standard deviation was about 0.1%, because they were 0.14%, 0.1%, and 0.07% at 1,000 rpm, 2,000 rpm, and 3,000 rpm, respectively. This is a result of the resolution of the duty ratio being designed to have a fine unit of $\pm 0.1\%$ because it determines the resolution of the speed control.

Because the speed errors were irregular over the load range, if the statistical standard deviation for each speed is chosen as the representative for the speed error, the proposed driver has a good speed error performance. As shown in Table 3, the speed error of 0.14% at 1,000 rpm was less than the results of [14] and [18] at the same speed, and similar to that of [15] at a higher speed. Above all, the speed error of 0.07% at 3,000 rpm showed the best performance considering that it was under sensorless control compared to previous works under sensed control.

V. Conclusion

This paper proposed an integrated and fully sensorless driver for PMSMs, operating without sensors, such as position, speed, current, and voltage sensors. The proposed driver is composed of a digital motor controller and analog pre-driver including a three-phase current sensing circuit. The implemented SMO algorithm estimated the back-EMF and calculated the rotor position using the drive voltage and measured current of the motor, and the speed was estimated and controlled using the rotor position. The pre-driver was designed using a level shifter and an isolation technique to be integrated with the motor controller, and the current sensing circuit was designed to sense the three-phase current simultaneously by the three independent ADCs. In the experiment with the IC fabricated using a 0.18 μm BCDMOS process, the operation and performance were evaluated using sensorless control, driving a 1,500 W motor through a three-phase inverter at 1,000 rpm, 2,000 rpm, and 3,000 rpm under a 5 N·m load. The driver showed a stable operation in spite of the variation in speed and

load, and has near a 1% efficiency difference over all load ranges at the rated speed, as compared to a commercial driver using a position sensor. In addition, it has a moderate speed ripple and low speed error of about 0.1%. Consequently, the proposed integrated driver has good performance for a PMSM drive with sensorless control.

References

- [1] M. Pacas, "Sensorless Drives in Industrial Applications," *IEEE Ind. Electron. Mag.*, vol. 5, no. 2, June 2011, pp. 16–23.
- [2] P.P. Acamley and J.F. Watson, "Review of Position-Sensorless Operation of Brushless Permanent-Magnet Machines," *IEEE Trans. Ind. Electron.*, vol. 53, no. 2, Apr. 2006, pp. 352–362.
- [3] P. Damodharan and K. Vasudevan, "Sensorless Brushless DC Motor Drive Based on the Zero-Crossing Detection of Back Electromotive Force (EMF) from the Line Voltage Difference," *IEEE Trans. Energy Convers.*, vol. 25, no. 3, Sept. 2010, pp. 661–668.
- [4] J. Shao, "An Improved Microcontroller-Based Sensorless Brushless DC Motor Drive for Automotive Applications," *IEEE Trans. Ind. Appl.*, vol. 42, no. 5, Sept. 2006, pp. 1216–1221.
- [5] H. Lee and J. Lee, "Design of Iterative Sliding Mode Observer for Sensorless PMSM Control," *IEEE Trans. Contr. Syst. Technol.*, vol. 21, no. 4, July 2013, pp. 1394–1399.
- [6] G. Wang, R. Yang, and D. Xu, "DSP-Based Control of Sensorless IPMSM Drives for Wide-Speed-Range Operation," *IEEE Trans. Ind. Electron.*, vol. 60, no. 2, Feb. 2013, pp. 720–727.
- [7] Z. Qiao et al., "New Sliding-Mode Observer for Position Sensorless Control of Permanent-Magnet Synchronous Motor," *IEEE Trans. Ind. Electron.*, vol. 60, no. 2, Feb. 2013, pp. 710–719.
- [8] V.D. Colli, R.D. Stefano, and F. Marignetti, "A System-on-Chip Sensorless Control for a Permanent-Magnet Synchronous Motor," *IEEE Trans. Ind. Electron.*, vol. 57, no. 11, Nov. 2010, pp. 3822–3829.
- [9] M.A. Hamida et al., "An Adaptive Interconnected Observer for Sensorless Control of PM Synchronous Motors with Online Parameter Identification," *IEEE Trans. Ind. Electron.*, vol. 60, no. 2, Feb. 2013, pp. 739–748.
- [10] K. Cheng and Y. Tzou, "Design of a Sensorless Commutation IC for BLDC Motors," *IEEE Trans. Power Electron.*, vol. 18, no. 6, Nov. 2003, pp. 1365–1375.
- [11] M. Carpaneto et al., "Dynamic Performance Evaluation of Sensorless Permanent-Magnet Synchronous Motor Drives with Reduced Current Sensors," *IEEE Trans. Ind. Electron.*, vol. 59, no. 12, Dec. 2012, pp. 4579–4589.
- [12] A. Khlaief et al., "A Nonlinear Observer for High-Performance Sensorless Speed Control of IPMSM Drive," *IEEE Trans. Power Electron.*, vol. 27, no. 6, June 2012, pp. 3028–3040.
- [13] J.W. Jung and Y.S. Koo, "Design of SCR-Based ESD Protection

Circuit for 3.3 V I/O and 20 V Power Clamp,” *ETRI J.*, vol. 37, no. 1, Feb. 2015, pp. 97–106.

- [14] F. Rodriguez and A. Emadi, “A Novel Digital Control Technique for Brushless DC Motor Drives,” *IEEE Trans. Ind. Electron.*, vol. 54, no. 5, Oct. 2007, pp. 2365–2373.
- [15] A. Sathyan et al., “An FPGA-Based Novel Digital PWM Control Scheme for BLDC Motor Drives,” *IEEE Trans. Ind. Electron.*, vol. 56, no. 8, Aug. 2009, pp. 3040–3049.
- [16] S.M. Lukic and A. Emadi, “State-Switching Control Technique for Switched Reluctance Motor Drives,” *IEEE Trans. Ind. Electron.*, vol. 57, no. 9, Sept. 2010, pp. 2932–2938.
- [17] L.O.A.P. Henriques et al., “Development and Experimental Tests of a Simple Neurofuzzy Learning Sensorless Approach for Switched Reluctance Motors,” *IEEE Trans. Power Electron.*, vol. 26, no. 11, Nov. 2011, pp. 3330–3344.
- [18] W. Sun et al., “Hybrid Motor Control Application with Moving Average Based Low-Pass Filter and High-Pass Filter,” *Int. Conf. Electr. Mach. Syst.*, Oct. 22–25, 2014, pp. 3123–3130.



Sewan Heo received his BS and MS degrees in electrical and electronic engineering from the Korea Advanced Institute of Science and Technology, Daejeon, Rep. of Korea, in 2005 and 2007, respectively. He joined ETRI in 2007, where he is currently a senior researcher. His research interests include power converters, synchronous motor drives, digital/analog control circuits design, and renewable energy conversion in power systems.



Jimin Oh received his BS degree in electrical and electronic engineering and his MS degree in electrical engineering from Kyoto University, Japan, in 2008 and 2010, respectively. Upon graduating, he joined ETRI as a researcher. His research interests include motor driver IC design, power management IC design, nonlinear dynamics, and MEMS.



Minki Kim received his BS degree in electrical engineering and computer science from Kyungpook National University, Daegu, Rep. of Korea, in 2008 and his MS degree in electrical engineering and computer science from Seoul National University, Rep. of Korea, in 2010. Since 2010, he has been working at ETRI as a researcher. His research interests include wide band-gap power devices and power control systems.



Jung-Hee Suk received his BS, MS, and PhD degrees in electronics engineering from Kyungpook National University, Daegu, Rep. of Korea, in 2001, 2003, and 2007, respectively. His doctoral research involved the H.264/AVC codec algorithm. He joined ETRI in February 2007 as a researcher and now works for the NT Convergence Components Research Department. His current research interests include multi-media codecs; parallel processing of media data; efficient architectures of SoC; recognition algorithms for smart vehicles and mobile terminals; and motor control systems.



Yil Suk Yang received his BS, MS, and PhD degrees in electronics engineering from Kyungpook National University, Daegu, Rep. of Korea, in 1989, 1994, and 2008, respectively. Before joining ETRI in 1999, he was with LG Semiconductor, Seoul, Rep. of Korea. Since 1999, he has worked at ETRI's Basic Research Laboratory, where he has been engaged in research on low power circuit design, high energy efficiency circuit design, and power electronics design.



Ki-Tae Park received his BS degree and MS degrees at the Department of Electrical Engineering from Seoul National University, Rep. of Korea, in 1995 and 1997, respectively. Since 1997, he had worked for Samsung Electronics, Co., Ltd., Suwon, Rep. of Korea until he founded Iron Device Corporation, Seoul, Rep. of Korea in 2008, where he is CEO. His interests include mixed signal system LSI design, audio power amplifier IC, and power electronics.



Jinsung Kim received his BS degree at the Department of Electrical Engineering from Konkuk University, Seoul, Rep. of Korea, in 1998. From 1998 to 1999, he had worked for Samsung Electronics, Co., Ltd., Suwon, Rep. of Korea. From 2009 to 2008, he had worked for Fairchild Korea, Co., Ltd., Bucheon, Rep. of Korea. Since 2008 he has worked at Iron Device Corp., Seoul, Rep. of Korea as a circuit designer. His interests include mixed signal system LSI design, class D audio amplifier, and power electronics.